AGU | ADVANCING EARTH AND SPACE SCIENCE

Geophysical Research Letters®

Diurnal Variations in the Aphelion Cloud Belt as Observed by the Emirates Exploration Imager (EXI)

Michael J. Wolff[1], Anton Fernando[2,3], Michael D. Smith[4], François Forget[5], Ehouarn Millour[5], Samuel A. Atwood[2,3], Andrew R. Jones[2], Mikki M. Osterloo[1], Ralph Shuping[1], Mariam Al Shamsi[6], Christian Jeppesen[2], and Charles Fisher[2]

[1]Space Science Institute, Boulder, CO, USA, [2]Laboratory for Atmospheric and Space Physics, University of Colorado Boulder, Boulder, CO, USA, [3]Space and Planetary Science Center, Khalifa University, Abu Dhabi, UAE, [4]NASA Goddard Space Flight Center, Greenbelt, MD, USA, [5]Laboratoire de Météorologie Dynamique, Paris, France, [6]Mohammed Bin Rashid Space Centre, Dubai, UAE

Abstract Observations by the Emirates eXploration Imager (EXI) on-board the Emirates Mars Mission are used to characterize the diurnal, seasonal, and spatial behavior of aphelion cloud belt during Mars Year 36 $L_S \sim 30°–190°$. Building from previous work with the Mars Color Imager (MARCI) onboard the Mars Reconnaissance Orbiter, we retrieve water ice extinction optical depth (τ_{ice}) with an uncertainty ± 0.0232 (excluding particle size effects). We connect EXI and MARCI using radiance and τ_{ice}. Zonal and meridional diurnal trends are analyzed over 6–18 hr Local True Solar Time. The retrievals show large morning-evening asymmetries about a minimum near 12 hr. The latitudinal distributions in early morning are extensive and particularly striking near mid-summer. Comparisons to the Mars Planetary Climate Model show reasonable agreement with basic diurnal behavior, but noticeable departures include too much water ice in early morning, the general latitudinal extent, and behavior at smaller scales like the volcanoes and other topographically distinct features.

Plain Language Summary Water ice clouds have important roles in the Martian atmosphere because they can influence weather and act as probes of important weather and climate processes. Using the camera on-board the Emirates Mars Mission, water ice clouds are studied for the first time throughout the Martian day and year at scales of 10–20 km around the planet. We study a key cloud structure called the aphelion cloud belt (ACB) that encircles the planet at low latitudes during the northern hemisphere spring and summer seasons. Using the camera images from this period, we examine how the ACB structure changes from morning through evening and throughout these two seasons. We developed a computer program that converts the brightness of a pixel into a measure of the cloud thickness. We find that the ACB clouds are much thicker and wide-spread in the early morning compared to other times of day; and are much more extant across the planet in the morning, particularly in mid-summer. We also compare to weather prediction programs and find important differences that will help scientists improve Mars weather forecasts for future research and missions.

1. Introduction

Water ice clouds are recognized to have a fundamental contribution to the Martian atmosphere through their formation processes and their roles in the atmospheric radiation budget (e.g., Clancy et al., 2017; Wolff et al., 2019; and references within). A necessary step in understanding the nature of their interactions with the overall atmospheric system is the observational characterization of the spatial (vertical and horizontal) and temporal (diurnal, seasonal) domains. Significant progress has been made in recent years with respect to the spatial domain and the seasonal variability. However, observations of the diurnal cycle have been limited to a small number of points on the surface from landed assets (i.e., Mars Exploration Rovers, Phoenix, Curiosity, Insight, Perseverance), and to a combination of limited local-times from sun-synchronous orbiters (Mars Global Surveyor, e.g., Smith (2004); Odyssey, e.g., Smith (2019); Mars Reconnaissance Orbiter (MRO), e.g., Wolff et al. (2019)) and a convolution of diurnal and seasonal timescale from orbiters with a precessing orbit (Viking, e.g.,Tamppari et al. (2003), Mars Express, e.g., Giuranna et al. (2021); Trace Gas Orbiter (TGO), e.g., Liuzzi et al. (2020)). An exception to the latter case is the MAVEN mission (e.g., Connour et al., 2017) which has obtained diurnal sampling of several regions on a sub-seasonal timescale. Consequently, a mission that provides globally-spatial coverage with diurnal

sampling accumulated on a short timescale (e.g., a week) across seasons offers new constraints on the physical processes involving clouds.

The Emirates Mars Mission (EMM), which arrived in orbit on 9 February 2021, has a science orbit that fills such a niche. Its near-equatorial orbit provides spatial coverage over much of the planet with a diurnal sampling of at least 3–4 local times over 7–10 days. There are two instruments onboard that sample the lower atmosphere, typically through column integrated optical depths: Emirates eXploration Imager (EXI; Jones et al. (2021)) and Emirates Mars InfraRed Spectrometer (EMIRS; Edwards et al. (2021)). By combining the their data, one captures the full diurnal cycle, and places constraints on the water-ice particle sizes. In addition, EMIRS can explicitly distinguish between water-ice and dust aerosols, while analysis of EXI data must adopt a dust column.

In this paper, we focus solely on EXI observations, naturally limited to daytime hours. Observations by EMIRS are described by Atwood et al. (2022); Smith et al. (2022). We briefly describe the instrument, the data set, and the analysis algorithm. The resulting retrievals of water ice optical depth are presented through highlights of the observed diurnal behavior of the aphelion cloud belt (ACB) structure from early spring through early fall in the northern hemisphere. Comparisons are also made to a Martian Global Circulation Model (MGCM).

2. Instrument-Data Set Description

EXI is a multi-band camera capable of taking 12-megapixel images, described in detail by Jones et al. (2021). Given the science orbit of EMM, EXI provides a spatial resolution of 2–4 km per native pixel with six discrete bands from the mid-ultraviolet through the visible. Radiometric fidelity is optimized while simplifying the optical design through the separation of the ultraviolet (UV) and visible (VIS) optical paths. The work here focuses on the "f320" band, nearly identical to the MARCI band 7 (Wolff et al., 2019) This band has a solar flux weighted-mean centroid of 321 nm, a Full-Width Half-Maximum of 24 nm, and a radiometric accuracy (and precision) better than 5%.

The principal observational mode of EXI is the so-called XOS-1 (XOS = eXi Observation Set), which includes the f320 band. Because there is a direct trade-off between data volume and number of observations, the f320 images are taken in a 2×2 binning mode, giving 4–8 km per pixel at nadir. Each image is processed to "Level 2A" (L2A), which includes a calibrated image and associated metadata such as latitude and longitude, photometric angles, range from surface. Keywords are included to transform the DN values to radiance and radiance factor (I/F). The L2A file is the starting point for the cloud retrieval. Availability of EXI products and documentation is described in the Data Availability Statement.

3. Retrieval Algorithm

The column-integrated ice extinction optical depth (τ_{ice}) retrieval is based on that developed for MRO/MARCI (Wolff et al., 2019). The algorithm uses large look-up tables to replace direct calls to a radiative transfer algorithm, offering a several-order-of-magnitude speed-up. Schematically, one specifies the atmospheric state and boundary conditions except for τ_{ice} and then employs multi-dimensional interpolation to provide a one-to-one, monotonic mapping between τ_{ice} and I/F. The pipeline consists of several discrete steps: (a) starting with the Level 2A product, calibrated Data Number values are converted to radiance factor (*I/F*); (b) the EMIRS dust retrievals and a Global Climate Model surface pressure map are used to specify those quantities for each pixel; (c) τ_{ice} is generated through two separate interpolation stages—a linear multi-dimensional and then a one-dimensional cubic spline. The tessellation of the look-up table is carefully chosen to keep the interpolation error below 1% (Wolff et al., 2019, Section 3.2); (e) in addition to the τ_{ice} image (which retains the observational geometry of the Level 2A image), images are created to provide a user with surface ice and data quality masks. The latter gives the reason(s) for any off-nominal result of the retrieval process (e.g., angles out of range). The ultimate product of this process is a Level 3 (L3) file, consisting of τ_{ice}, the two masks, and associated metadata to provide information on key files and parameters used in the pipeline process. Below, we provide additional detail for aspects of the input parameters generation that differ from those of Wolff et al. (2019).

3.1. Dust Column

We use a contemporaneous dust climatology constructed from the EMIRS observations (Smith et al., 2022). To improve the coverage statistics, we combine all the EMIRS retrievals for Local True Solar Times (LTST)

06–18 hr into a single bin. Because Smith et al. do not identify any diurnal trends of dust, we cannot do any more than include the general dust error in our error analysis. We adopt a cross section-weighted mean radius (r_{eff}) of 1.5 μm and the dust model of Wolff et al. (2009, 2010) to convert the EMRIS dust extinction optical depth to one appropriate for the EXI f320 band. This approach provides a direct scaling of the extinction optical depth at 9.3 μm to that at 320 nm: $\tau_{dust}(EXI) = 1.68\ \tau_{dust}(EMIRS)$. Allowing for a 10% uncertainty in r_{eff} (e.g., Kahre et al., 2017) results (coincidentally) in ∼10% uncertainty in the scaling factor, that is, for $r_{eff} = 1.35$ μm, $\tau_{dust}(EXI) = 1.84\ \tau_{dust}(EMIRS)$ and for $r_{eff} = 1.65$ μm, $\tau_{dust}(EXI) = 1.56\ \tau_{dust}(EMIRS)$.

3.2. Surface Reflectance Model

While we adopt the basic Hapke model for MARCI band 7 and its spatial variations (Wolff et al., 2019), we scale the w parameter by 1.07 to account for the differences in the radiometric calibration, which will be discussed further in Section 4.1. Briefly, given the way that the surface reflectance values were derived by Wolff et al. (2019), an error in the radiometry will alias proportionally into the derived w value, that is, using only moderate photometric angles, conditions with low-to-moderate dust columns and no water ice. Not surprisingly, the error in the surface reflectance produces non-negligible effects only for small water-ice optical depths, which decrease from ∼0.02 for $\tau_{ice} = 0$ to 0.005 for $\tau_{ice} = 0.1$. Practically, the scaling provides a zero-point correction: regions of no or very little water ice for a given season now provide similar τ_{ice} values in both MARCI and EXI data sets.

3.3. Limitation of τ_{ice} Detection and Surface Ice Filter

The retrieval cannot discriminate between atmospheric and surface ice, nor between water and carbon dioxide ice. Given the seasonal, latitude, and local time ranges considered here ($L_S = 30 - 190°$, ±50°N, 6–18 hr Local True Solar Time (LTST)), all the derived τ_{ice} is attributed to the atmosphere and associated with H_2O. CO_2 clouds present within the analyzed data set are likely to be optically thin, particularly given when included in the 2×2 binning of the EXI images, for example, Vincendon et al. (2011). However, we note that the L3 products contain an "ice mask" that provides guidance on the potential for surface ice in a given pixel. The mask is derived from a series of EMIRS observations of surface temperature over several orbits around the EXI observation, and is further described in the EXI Data Guide (Data Availability Statement).

3.4. Uncertainties

The general retrieval uncertainty is calculated following the prescription of Wolff et al. (2019, Table 3). We use a conservative value of 10% for the optical depth error (Smith et al., 2022), 10% for the optical depth scaling factor as discussed above (giving a total dust uncertainty of 20%), and a radiometric error of 5%. Using the Monte Carlo algorithm for all tabulated error sources, we derive an uncertainty of ±0.023; very similar to that for the MARCI retrieval.

A more difficult error term is that associated with the water ice particle size. We simply adopt the analysis of Wolff et al. (2019), which assumes the clouds have $r_{eff} = 3$ μm. The retrieved τ_{ice} is estimated to be ∼30%–40% too high if the clouds actually have particles with $r_{eff} = 1.5$ μm, but τ_{ice} would be slightly too low (less than 10%) if the clouds really have $r_{eff} = 4$–6 μm.

4. Results

The retrieval is applied to all pixels within the L2A images with incidence and emergence angles ≤75° obtained from $L_S \sim 30°$ (shortly before the official start of the prime science mission) through $L_S \sim 190°$ (early northern fall, and the expected annual dissipation of the ACB), which are in Mars Year (MY) 36. In our analyses, we insert the characteristics of each valid retrieved pixel into a simple database. This simplicity comes with a modest performance cost given the file size of ∼4 Gigabytes, but it allows us to generate products with arbitrary spatial and temporal binning.

4.1. Connection to MARCI

Given the long temporal baseline of the MARCI data set, it is useful to verify the consistency (and connection) of the two data sets. One way is a direct comparison of EXI and MARCI radiance observations for overlapping pixels. Through experimentation, we optimize a set of parameters that define a pixel match: Δtime ≤20 min,
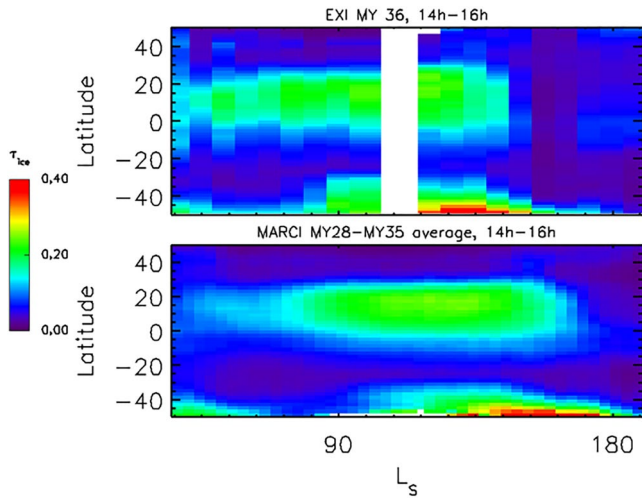
Figure 1. Comparison of Emirates Exploration Imager (EXI) to Mars Color Imager (MARCI) extinction optical depth for Local True Solar Times (LTST) 14–16 hr. The EXI data are from MY36, while the MARCI data are average of MY28-45 (Wolff et al., 2019). The EXI data are binned 1.5° in latitude and 7.5° in L_S. The gap in the EXI data around L_S 110° is caused by a combination of solar conjunction and spacecraft safing events. The MARCI data are those used by Wolff et al. (2019), Figure 14, and binned 1° in latitude and 6.5° in L_S.

Δincidence, emergence, phase $\leq 4°$, and Δlatitude, longitude $\leq 0.4°$. Time and location restrictions enforce the viewing of the same effective column/ surface, while the angles minimize differences associated with radiative transfer effects. In the UV, the former constraint is particularly key because clouds moving into or out of a pixel introduce large photometric effects. The chosen angles minimize scatter while maximizing overlaps, that is, more restrictive limits do not further reduce scatter but definitely reduce overlaps. Despite the large number of images, we find only four sets of observations ranging from July 2021 through March 2022 that meet the above requirements, providing about 50 cases of overlapping pixels. The sample of relative (EXI I/F minus MARCI I/F) differences has a mean difference of 0.072 ± 0.004, indicating that for EXI-MARCI observations under identical conditions, a MARCI pixel will be 7% darker than one of EXI. This is the origin of the 1.07 factor for surface reflectance.

A second useful comparison is the zonal behavior for τ_{ice} at 14–16 hr LTST during the ACB season, as is shown in Figure 1. Each instrument data set shows very similar τ_{ice} values and behavior. Notable differences between them are related to two factors: (a) the MARCI data are heavily weighted toward the mean time LTST (15h00) while EXI data are essentially uniformly-weighted across the LTST interval. This makes the largest difference early in the ACB formation; (b) MY36 is different, having large scale dust activity $L_S \sim 145°$–$155°$ (January 2022) during the decay phase of the ACB, which is not the case for MY28-34 in the MARCI average which show only very small interannual variations (Wolff et al., 2019).

4.2. Diurnal Variations

Having provided a retrieval comparison with respect to MARCI data, we move to analyze the local time behaviors observed by EXI.

4.2.1. Zonal

Figure 2 illustrates the diurnal variations in the zonal mean τ_{ice}. An inspection of the panels reveals a few obvious trends:

1. The period of minimum (zonal) cloudiness of the ACB appears to be a ~12 hr, with symmetry seen ±2 hr about this point. This symmetry is broken as the intervals move further away from noon, i.e., 8–10 hr is cloudier than
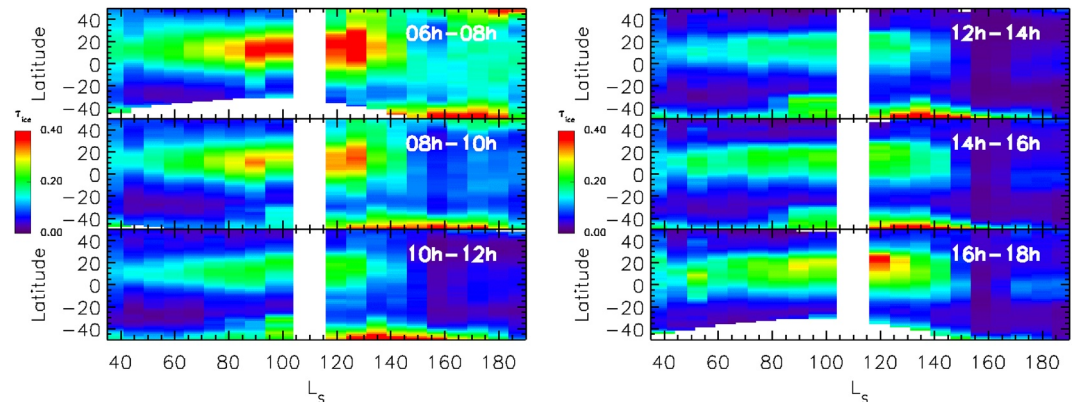

Figure 2. Emirates Exploration Imager (EXI) morning (left) and afternoon (right) τ_{ice} zonal mean behavior. The data are binned as in Figure 1. Two hours in local time represents a trade-off between Local True Solar Times (LTST) resolution and L_S coverage. The missing latitudinal coverage in the upper left and the lower right panels is due to the periapsis of the Emirates Mars Mission (EMM) being in the Northern hemisphere.

14–16 hr. The early-to-mid morning is significantly cloudier than mid-afternoon to early evening periods. We note that the bins were chosen for MARCI comparisons and uniform sampling for 6–18 hr. When the binning is constructed around an 11–13 hr interval, one sees a minimum value with respect to neighboring diurnal blocks.

2. In addition to the early morning ACB clouds being significantly thicker, they possess a greater latitudinal extent than is found in the evening block. This trend manifests dramatically after the regional dust activity ($L_S \sim 145°$–155°), though perhaps no longer technically part of the ACB season. In fact, the morning clouds never seem to completely disappear during this period.

3. A final trend to mention is that along the southern boundary of the figures, though outside the ACB. The τ_{ice} here is a combination of the south polar hood and the cloudiness of the Hellas basin. Not surprisingly, a seasonal dependence can be seen in the diurnal patterns.

The EMM orbit allows for the clear delineation of the diurnal-seasonal characteristics. However, limited aspects of the above trends have been previously reported from other missions. For example, the general diurnal-zonal behavior of the ACB evident in the Hubble Space Telescope (very sparse) observations is consistent with that observed by EXI, at least when one considers them in a zonal mean sense (e.g., Wolff et al., 1999, Figures 7–9). Similar mid-to-late afternoon trends are documented in analyses of the Odyssey (Smith, 2019) and the MRO (Wolff et al., 2019) data sets. The strong early morning-early evening asymmetry seen by EXI is quite consistent with the cloudiness trends observed by Viking (Tamppari et al., 2003), the TGO sunrise-sunset terminator occultation profiles (Liuzzi et al., 2020) and in highly-binned (local time and season) Planetary Fourier Spectrometer data column-integrated optical depths (Giuranna et al., 2021).

4.2.2. Longitude-Latitude

A zonal-mean can suppress even large meridional variations. As can be seen in Figure 3, this is certainly the case for water ice clouds. The choose of 3 hr LTST bins is necessary to provide more complete spatial coverage without having to appreciably larger L_S bins. As with the zonal figure, an examination of the panels finds some basic patterns:

1. The ACB is most continuous near northern summer solstice for all LTST bins. The upper right-hand time step in Figure 3 is chosen specifically to illustrate this point.

2. The period of peak activity, which one might loosely define as a convolution of optical depth and spatial extent, occurs near mid-summer, $L_S \sim 130°$, similar to that from the zonal plots. The diurnal variations of the meridional structure are quite striking and the morning-evening asymmetry is more apparent than in other time periods.

3. Cloud activity continues during the large scale dust event of $L_S \sim 145°$–155°, though it appears largely suppressed throughout much of the day. Considering the abrupt cut-off of the ACB for EXI compared to that for MARCI in Figure 1, it seems likely that this suppression is due mainly to the dustier atmosphere associated with the regional event. Clouds also reappear in the afternoon after $L_S \sim 170°$ at levels consistent with those of the MARCI data. This date does corresponds to the dust levels observed by EMIRS returning to those before the event (Smith et al., 2022, Figure 1). The omitted LTST bin of 9–12 hr is very similar to that for 12–15 hr, indicating a drop-off that is relatively abrupt after the 8–9 hr period.

There is essentially no published observational analog for the coverage offered by EMM, and demonstrated in Figure 3. However, MGCMs offer a basis for further comparison.

5. Comparison to Global Climate Models

A fundamental motivation for the EXI cloud retrievals is the creation of products that characterize the diurnal cycle to constrain MGCMs (Almatroushi et al., 2021; Amiri et al., 2022). We are taking the first step in that direction by comparing EXI τ_{ice} retrievals to the output of an MGCM available in the Mars community that is the model developed at the Laboratoire de Météorologie Dynamique (LMD) in collaboration with several European teams (LATMOS, IAA Granada, University of Oxford, The Open University) (Forget et al., 1999), which has recently been renamed the Mars Planetary Climate Model (MPCM). A detailed overview of the model, including the current implementations of the dust and water cycles, can be found in Navarro et al. (2014). For comparision to the EXI data, the MPCM is run on a $1° \times 1°$ grid with radiatively-active dust and water ice particles, and an average dust climatology scenario, that is, no global or unique large scale dust events, such as that occurred in MY36 and mentioned above.

Figure 4 (TOP) shows the MPCM zonal mean of the τ_{TES} parameter, and (BOTTOM) the spatial extent for two of the seasonal periods from the EXI figures. The output is binned 5° in L_S using the same LTST ranges as EXI.
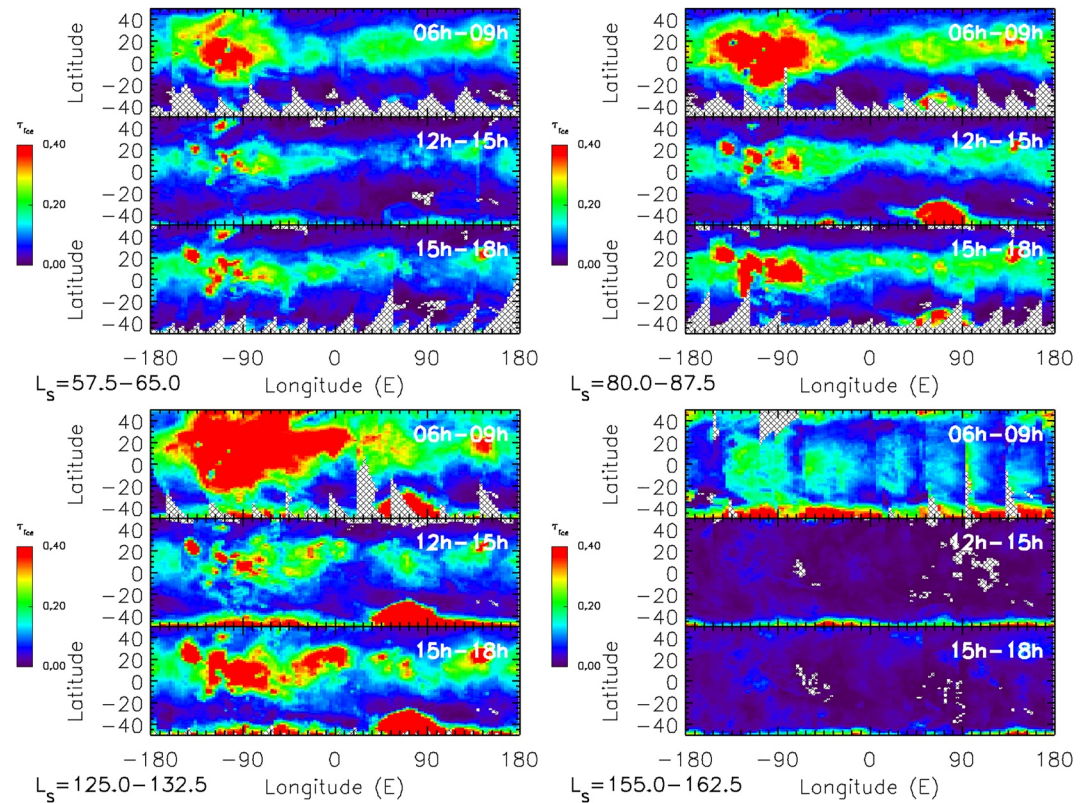
Figure 3. Spatial Extent of τ_{ice} near aphelion (late northern spring, top left), near summer solstice (top right), near the peak of aphelion cloud belt (ACB) cloud activity (bottom left), and near the end of the regional dust event (bottom right) The Emirates Exploration Imager (EXI) retrievals are binned $3° \times 1.5°$ (lng-lat) and $7.5°$ in L_S. Three-hour Local True Solar Times (LTST) bins are necessary to get reasonable spatial coverage. The missing data is due to a combinations the orbit periapsis being in the northern hemisphere and a combination of solar conjunction and spacecraft safing events. There are some artifacts in the dust storm time step due to non-uniform coverage across longitudes.

τ_{TES} is meant to be analogous to the Thermal Emission Spectrometer water ice 12.1 μm absorption optical depth retrieval (e.g., Smith, 2004). In order to compare them directly to EXI retrievals, one needs to scale the τ_{TES} values by the ratio of the extinction cross section at 320 nm to the absorption cross section at 12.1 μm. Here, that ratio is 1.8 for $r_{eff} = 3$ μm ice particles. Thus, the maximum of the color bar has been scaled by 1.8 so that the same color represents an identical amount of water ice in both the EXI and MPCM figures (given the indicated assumptions). For other particle sizes: $r_{eff} = 1.5$ μm, $\tau_{ice} = 2.9\tau_{TES}$; and for $r_{eff} = 6.0$ or 8.0 μm, $\tau_{ice} = 1.5\tau_{TES}$.

Comparing the EXI and MPCM optical depths highlight areas of both successful modeling and potential improvement. The exaggeration of the modeled south polar hood has been previously identified (e.g., Wolff et al., 2019). Thus, we confine our comments to the ACB structure.

1. Allowing for the regional dust activity in the EXI data set, MPCM reproduces reasonably well the general diurnal trends in both zonal and spatial products, particularly in the afternoon. This includes a morning-evening asymmetry, though the clouds do not seem to dissipate as quickly in the model. Though not shown here, the model shows a minimum cloudiness near 13 hr.
2. The broad-scale spatial structure of the ACB produced by the MPCM agrees well with that observed by EXI. Reasonable agreement also occurs between the scaled optical depth values (here, the colors in Figures 2 and 4) at low and moderate τ_{ice} regions.
3. The model does produce too much water ice in the early morning, has a wider range of latitudes with the thicker clouds, and over-produces in general near the peak of the ACB activity (at all LTST); Figure 4.
4. Comparing Figures 3 and 4, one can see interesting differences in the details of the ACB spatial structure at smaller scales as well, including the volcanoes; particularly Olympus Mons and the Tharsis ridge (a subject of future work).
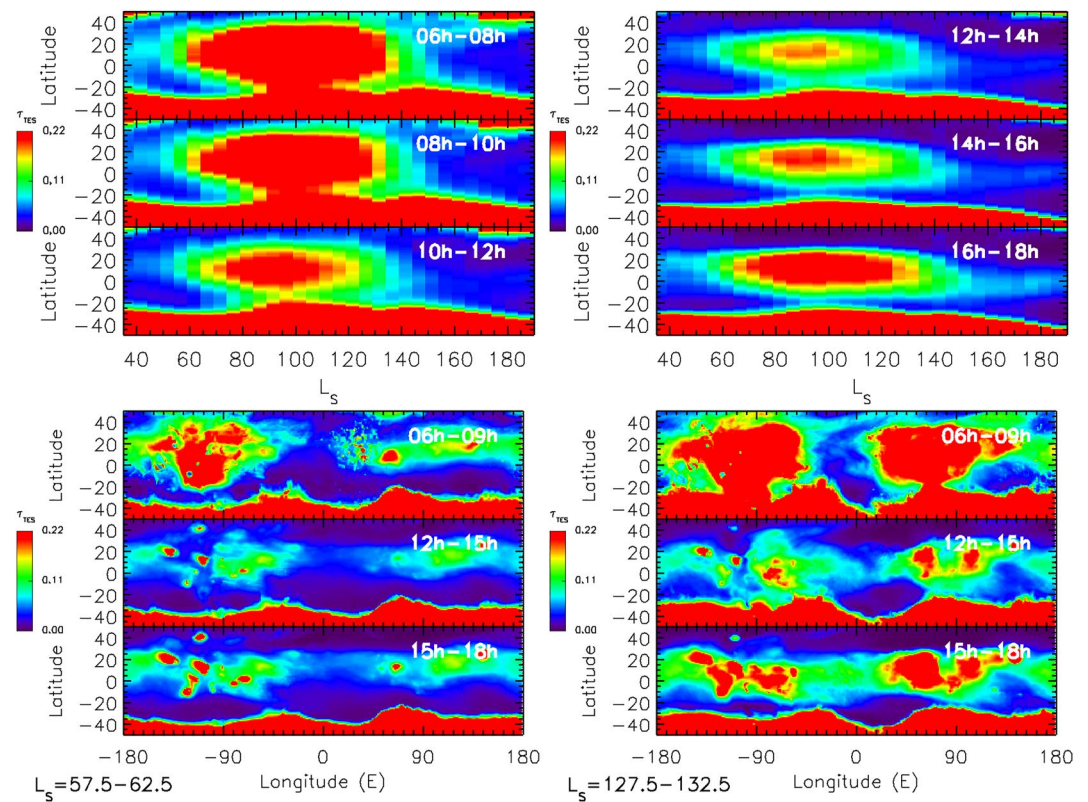
Figure 4. Mars Planetary Climate Model (MPCM) results: TOP: morning (left) and afternoon (right) τ_{TES} zonal mean behavior; BOTTOM: Spatial extent of τ_{TES} near aphelion (late northern spring, left) and near the peak of aphelion cloud belt (ACB) cloud activity (right) The data are 1° in latitude and binned ~5° in L_S, where the latter is to better represent the Emirates Exploration Imager (EXI) observations. The color bar has been scaled so that the same color in the EXI and MPCM figures represents the same amount of ice for $r_{eff} = 3$ μm.

While the areas of success of the model are encouraging, it is those in need of improvements that likely represent the more interesting aspects of the model-observation comparisons. It is the differences which provide the motivating avenues for further exploration of the physics involved. Consequently, the growing EXI (and general EMM) data set will continue to offer the opportunity to improve our understanding of the martian atmosphere.

6. Summary

We developed a retrieval process using the EXI f320 images to measure the water ice optical depth in the martian atmosphere. A validation/consistency check using MARCI is done through direct comparisons of radiance and τ_{ice}. Combining EXI with the EMM orbit, which effectively samples most of the planet and the daytime diurnal cycle over a period of about 10 days, we explore the diurnal behavior of the ACB over the range of early northern spring through early fall. Although the occurrence of a large regional dust storm during the decay phase of the ACB perturbed the observed behavior, the average seasonal behavior of the zonal τ_{ice} is not surprising. However, the observed diurnal variations include a large morning-evening asymmetry about a minimum cloudiness point near 12 hr. In addition, the latitudinal distribution of the early morning clouds are quite extensive even during the regional dust storm, which effectively suppress the clouds throughout the rest of the day. One also finds that the ACB is most continuous in longitude for all observed LTST near northern summer solstice, while being most active (optical depth and latitudinal extent) near mid-summer. In fact, the latitudinal extent of the morning clouds near mid-summer is quite striking compared to that observed in the afternoon, that is, by EXI and by previous missions. The behavior of the ACB reasonably reproduced by the MPCM in terms of basic diurnal behavior of spatial and seasonal trends. Noticeable departures manifest as too much water ice in the model during the early morning through both larger latitudinal extents and higher peak optical depths. Model-observation difference are also seen at smaller scale for regions like the volcanoes and other topographically distinct features that do not

simply follow the trends enumerated above. These particular differences are currently being analyzed by others members of the EMM science team. In a similar vein, the work reported here represents only a small fraction of the seasonal and spatial coverage obtained at the point of this writing. Clearly, many additional investigations await, including the use of the EXI data set for synergistic collaborations with EMIRS and EMUS, as well as with other missions such as MRO, TGO, and the Curiosity and Perseverance rovers. Given the public nature of the EMM data, including the derived (L3) products, such projects are accessible to the entire community.

Data Availability Statement

Data from the Emirates Mars Mission (EMM) are freely and publicly available on the EMM Science Data Center (SDC, http://sdc.emiratesmarsmission.ae). This location is designated as the primary repository for all data products produced by the EMM team and as the long-term repository as required by the UAE Space Agency. The data available (http://sdc.emiratesmarsmission.ae/data) include ancillary spacecraft data, instrument telemetry, Level 1 (raw instrument data) through Level 3 (derived science products), quicklook products, and data users' guides to assist in the analysis of the data. Following the creation of a free login, all EMM data are searchable via parameters such as product file name, solar longitude, acquisition time, sub-spacecraft latitude, longitude, instrument, data product level.

Data product filenames follow a standard convention:

`emm_<Instrument>_<DataLevel><StartTimeUTC>_<OrbitNumber>_<Mode>_<Description>_<KernelLevel>_<Version>.<FileType>`.

EXI data and users guides are available at:

https://sdc.emiratesmarsmission.ae/data/exi.

EMIRS data and users guides are available at:

https://sdc.emiratesmarsmission.ae/data/emirs.

The Mars Planetary Climate Model (MPCM) is available from http://www-mars.lmd.jussieu.fr/; revision 2776 of the MPCM was used for this work.

References

Almatroushi, H., AlMazmi, H., AlMheiri, N., AlShamsi, M., AlTunaiji, E., Badri, K., et al. (2021). Emirates Mars mission characterization of Mars atmosphere dynamics and processes. *Space Science Reviews*, *217*(8), 89. https://doi.org/10.1007/s11214-021-00851-6

Amiri, H. E. S., Brain, D., Sharaf, O., Withnell, P., McGrath, M., Alloghani, M., et al. (2022). The Emirates Mars mission. *Space Science Reviews*, *218*(1), 4. https://doi.org/10.1007/s11214-021-00868-x

Atwood, S. A., Smith, M. D., Badri, K., Edwards, C. S., Christensen, P. R., Wolff, M. J., et al. (2022). Diurnal variability in EMIRS daytime observations of water ice clouds during Mars aphelion-season. *Geophysical Research Letters*, *49*(15), e2022GL099654. https://doi.org/10.1029/2022GL099654

Clancy, R. T., Montmessin, F., Benson, J., Daerden, F., Colaprete, A., & Wolff, M. J. (2017). Mars clouds, in the atmosphere and climate of Mars. In R. M. Haberle, R. T. Clancy, F. Forget, M. D. Smith, & R. W. Zurek (Eds.), (pp. 42–75). https://doi.org/10.1017/9781139060172.005

Connour, K., Schneider, N., Forget, F., Deighan, J., Jain, S., Pottier, A., et al. (2017). Mars topographic clouds: MAVEN/IUVS observations and LMD MGCM predictions. *AGU fall meeting abstracts*, *2017*, P23D–P2753.

Edwards, C. S., Christensen, P. R., Mehall, G. L., Anwar, S., Tunaiji, E. A., Badri, K., et al. (2021). The Emirates Mars mission (EMM) Emirates Mars InfraRed spectrometer (EMIRS) instrument. *Space Science Reviews*, *217*(7), 77. https://doi.org/10.1007/s11214-021-00848-1

Forget, F., Hourdin, F., Fournier, R., Hourdin, C., Talagrand, O., Collins, M., et al. (1999). Improved general circulation models of the Martian atmosphere from the surface to above 80 km. *Journal of Geophysical Research*, *104*(E10), 24155–24176. https://doi.org/10.1029/1999je001025

Giuranna, M., Wolkenberg, P., Grassi, D., Aronica, A., Aoki, S., Scaccabarozzi, D., et al. (2021). The current weather and climate of Mars: 12 years of atmospheric monitoring by the planetary Fourier spectrometer on Mars express. *Icarus*, *353*, 113406. https://doi.org/10.1016/j.icarus.2019.113406

Jones, A. R., Wolff, M., Alshamsi, M., Osterloo, M., Bay, P., Brennan, N., et al. (2021). The Emirates exploration imager (EXI) instrument on the Emirates Mars mission (EMM) hope mission. *Space Science Reviews*, *217*(8), 81. https://doi.org/10.1007/s11214-021-00852-5

Kahre, M. A., Murphy, J. R., Newman, C. E., Wilson, R. J., Cantor, B. A., Lemmon, M. T., & Wolff, M. J. (2017). The Mars dust cycle. In R. M. Haberle, R. T. Clancy, F. Forget, M. D. Smith, & R. W. Zurek (Eds.), *Asteroids, comets, meteors—ACM2017* (pp. 229–294). https://doi.org/10.1017/9781139060172.010

Liuzzi, G., Villanueva, G. L., Crismani, M. M. J., Smith, M. D., Mumma, M. J., Daerden, F., et al. (2020). Strong variability of Martian water ice clouds during dust storms revealed from ExoMars Trace Gas orbiter/NOMAD. *Journal of Geophysical Research*, *125*(4), e06250. https://doi.org/10.1029/2019JE006250

Navarro, T., Madeleine, J.-B., Forget, F., Spiga, A., Millour, E., Montmessin, F., & Määttänen, A. (2014). Global Climate Modeling of the Martian water cycle with improved microphysics and radiatively active water ice clouds. *Journal of Geophysical Research: Planets*, *119*(7), 1479–1495. https://doi.org/10.1002/2013JE004550

Smith, M. D. (2004). Interannual variability in TES atmospheric observations of Mars during 1999–2003. *Icarus*, *167*(1), 148–165. https://doi.org/10.1016/j.icarus.2003.09.010

Smith, M. D. (2019). Local time variation of water ice clouds on Mars as observed by THEMIS. *Icarus*, *333*, 273–282. https://doi.org/10.1016/j.icarus.2019.06.009

Smith, M. D., Badri, K., Atwood, S. A., Edwards, C. S., Christensen, P. R., Wolff, M. J., et al. (2022). EMIRS observations of the aphelion-season Mars atmosphere. *Geophysical Research Letters*, *49*(15), e2022GL099636. https://doi.org/10.1029/2022GL099636

Tamppari, L. K., Zurek, R. W., & Paige, D. A. (2003). Viking-era diurnal water-ice clouds. *Journal of Geophysical Research*, *108*(E7), 5073. https://doi.org/10.1029/2002JE001911

Vincendon, M., Pilorget, C., Gondet, B., Murchie, S., & Bibring, J.-P. (2011). New near-IR observations of mesospheric CO_2 and H_2O clouds on Mars. *Journal of Geophysical Research*, *116*, E00J02. https://doi.org/10.1029/2011JE003827

Wolff, M. J., Clancy, R. T., Kahre, M. A., Haberle, R. M., Forget, F., Cantor, B. A., & Malin, M. C. (2019). Mapping water ice clouds on Mars with MRO/MARCI. *Icarus*, *332*, 24–49. https://doi.org/10.1016/j.icarus.2019.05.041

Wolff, M. J., James, P. B., Todd Clancy, R., & Lee, S. W. (1999). Hubble Space Telescope observations of the Martian aphelion cloud belt prior to the Pathfinder mission: Seasonal and interannual variations. *Journal of Geophysical Research*, *104*(E4), 9027–9042. https://doi.org/10.1029/98JE01967

Wolff, M. J., Smith, M. D., Clancy, R. T., Arvidson, R., Kahre, M., Seelos, F., et al. (2009). Wavelength dependence of dust aerosol single scattering albedo as observed by the Compact Reconnaissance Imaging Spectrometer. *Journal of Geophysical Research*, *114*(E9), E00D04. https://doi.org/10.1029/2009JE003350

Wolff, M. J., Todd Clancy, R., Goguen, J. D., Malin, M. C., & Cantor, B. A. (2010). Ultraviolet dust aerosol properties as observed by MARCI. *Icarus*, *208*(1), 143–155. https://doi.org/10.1016/j.icarus.2010.01.010